



**Universiteit
Leiden**
The Netherlands

A Cell-Based Model of Angiogenesis Suggests That Vascular Stabilisation Can Result From Flow-Based Inhibition of Chemotaxis

Richard Kok

Student ID	s2684047
Date	27/09/2021
Specialisation	Bioinformatics
1st supervisor	Prof. dr. R.M.H. Merks ^{1,2}
2nd supervisor	Dr. K.J. Wolstencroft ³

Master's Thesis in Computer Science
Leiden Institute of Advanced Computer Science (LIACS)

¹ Mathematical Institute (MI)

² Institute of Biology Leiden (IBL)

³ Leiden Institute of Advanced Computer Science (LIACS)

Abstract

Angiogenesis, the process of blood vessel sprouting and remodelling from existing vessels, is a process of large medical concern. Research shows that the vascular network remodels itself during the process of angiogenesis under the influence of blood flow, through sensing endothelial wall shear stress (WSS), where endothelial cells (ECs) migrate up the flow gradient such that high flow vessels are stabilised whereby its cells take on a quiescent state. We propose the hypothesis that the cellular migration might result from flow-based inhibition of chemotaxis. Specifically, it is our objective to investigate whether the inhibition of chemotaxis by flow velocity is sufficient to promote cellular migration. Biologically, we assume that wall shear stress can be sensed and relayed through VE-cadherin, VEGFR2 and PECAM1. These mechanisms could potentially be coupled through NO and ROS which have been shown to influence chemotaxis sensitivity. We furthermore assume that endothelial cells, in addition to sensing, also secrete chemoattractants. The Cellular Potts Model (CPM) will be used to simulate the process of flow-based remodelling. We expand the two-dimensional model with haemodynamics, by means of the Hagen-Poiseuille equation. The equation is a physical law modelling pressure difference, from which other haemodynamics can be extracted, on the assumption of laminar flow. The assumption of laminar blood flow has been shown to be justified in capillaries. The CPM model is computationally modelled in the Tissue Simulation Toolkit, an open source C++ library for simulating vascular morphogenesis. Whereas previous cell-based models lacked the simulation of haemodynamic, our model simulates blood flow dynamics and derives these computations in an efficient manner, whereby the necessary steps of segmentation and skeletonisation of the vasculature are solved through a dynamic process. Simulations were performed where the flow velocity has been calculated throughout the vasculature, with the chemotaxis component linearly inhibited with flow velocity. Results have shown that flow-based inhibition of chemotaxis leads to clustering of the vascular network into small and large vessels, the latter resembling arterioles. ECs in smaller vessels remain motile and frequently migrate into larger high flow vessels where they take on a quiescent state. The arising arterioles furthermore act as stable vessels that span over the CPM lattice and show a high volume flow rate. Our simulations quantitatively reproduce vascular stabilisation by means of structural vascular differentiation through flow-based inhibition of chemotaxis. We recommend both the application of dynamic updates and make the proposal for future researchers to take on the question whether flow-inhibited chemotaxis also leads to vascular remodelling with in vitro or in vivo research models.

1 Introduction

Biological problem

In this research we strive to uncover how blood flow dynamics can motivate the formation of a vascular tree from the primitive vascular plexus. First we will place the primitive vascular plexus in its proper biological context. Vasculogenesis establishes the first vascular network, which is defined as the primitive vascular plexus [1]. Whilst it is developing early signs of remodelling are visible, where remodeling is defined as the functional adaptations the network makes, without measurably affecting the total network span, through rearranging the number and/or location of vascular segments. In the process of vascular remodelling vessels can either fuse into bigger vessels, disappear or remodel into smaller segments. The arising second vascular plexus is hereby more complexly structured and can through angiogenesis be further expanded [1]. In this research we refer when speaking of angiogenesis also to the remodelling of the second vascular plexus.

Endothelial cells (ECs), which form the single-layer tissue lining the blood vessels, can sprout from pre-existing vascular networks through a process called angiogenesis. Angiogenesis occurs during physiological processes as wound healing and endurance exercise [2], as well as in other metabolically demanding conditions. To assist in the sprouting events, the cells take on a specialised role of either a tip or stalk cell. The former pro-explorative, the latter ensuring connectivity. Hypoxic regions incite pathological vascular sprouting through vascular-endothelial growth factor (VEGF) which shifts the balance in favour of the explorative tip cells by making the endothelial cells hyperactive through their extensions of multiple filopodia and loosened cell-cell adhesion [3].

All sprouting events, physiological and pathological, are characterised by endothelial cells forming new vessels in response to chemokines and growth factors [4]. After the sprouting phase remodelling occurs, at least in the physiological case, with remodelling predominantly occurring through vessel regression, as opposed to apoptosis, during mouse developmental angiogenesis [5]. Blood flow tunes hereby the remodelling where EC migrate up the flow gradient to stabilise high flow vessel segments, [5] where ECs in stabilised segments take on a quiescent state, with only 0.01 percent of the cells dividing in the healthy adult [3].

Stabilisation of high flow vessel segments, driven by functional vascular remodelling, is needed such that these metabolically important vascular stems are less susceptible to cease in supporting their dependent capillary crowns with metabolites. Imbalances between sprouting and remodelling, for example accelerated remodeling, premature pruning, reduced pruning or delayed remodeling, can negatively affect the physiological state and even induce tumour metastasis [6]. Notably, research suggest that unresolved vascular remodeling plays a key role in virtually all vascular diseases [7]. Desired advances with respect to forementioned issues makes research on angiogenic remodelling of pressing concern, where we use the term broadly in this research to also encompass the remodelling events associated to the formation of the second vascular plexus.

Research Question

Research has uncovered pathways for vascular morphogenesis [4]. Vially, through regression events blood vessels remodel themselves such that the vascular network before remodelling, the primitive plexus, can mature in a more stabilised and mature network optimised for metabolic demand. This remodelling occurs as a response to haemodynamic forces, predominantly flow-induced shear stress [5][8]. The shear stress induces cellular migration from low to high flow segments.

Gödde & Kurz [9] and Welter & Rieger [10] proposed endothelial wall shear stress (WSS) rather than volume flow rate or pressure distribution as the haemodynamic criterion for vessel stability. WSS through increased blood flow in small vessels triggers local inflammatory responses which leads, amongst others, to VEGF production [11]. The vasculature initiates the remodelling phase and stabilises in the order of days to weeks in mouse models through enlargement of the high flow vessels and de novo formation of sprouts which reduces vascular wall inflammation [7]. In our research we classify stabilising as the vasculature structurally accommodating to haemodynamic demands.

WSS is intuitively more plausible than blood flow rate as endothelial cells receive more information concerning shear stress exerted on their walls than on the total blood volume flowing through a vessel. In addition, relating regression events to flow rate would imply survival of only the thickest vessels as flow rate scales with the fourth power of the vessel radius. Also, Bernabeu et al. [12] linked endothelial shear stress gradients with regression events between postnatal day five and six in the murine retinal vascular plexus. Importantly for stabilisation of the vascular network, vessels

under low flow conditions are kept open through Wnt signaling which reduces endothelial shear sensitivity [8]. In addition mechanosensitive transcription factors, endothelial adhesion molecules, growth factors and other ligands have been found to play a role in endothelial migration events [4][5][8]. Evidently, various factors are of influence in vascular stabilisation. As such we distinguish between primary and secondary processes. A stepping stone would be to find the minimal set of causal factors that prove to be sufficient in stabilising the primitive plexus. Under the assumption that WSS-induced vessel regression promotes vascular stabilisation, we desire to uncover the unifying molecular or cellular processes sufficient to induce stabilisation of high flow vessel segments as a consequence of WSS.

VEGF production under WSS has been shown to attract ECs. An increased inward flow of ECs into high flow vessels might result in the same structural outcomes as a decreased outward flow of ECs from these same vessels. Therefore, our primary goal is to investigate, through computational modelling, whether instead of increasing VEGF secretion, the decreasing of VEGF sensitivity in high flow vessels might result in vascular stabilisation.

Biological knowledge

Before ECs start to migrate in the process of vascular remodelling they polarize themselves against the blood flow. This polarization occurs as a response to shear stress induced by high flow segments, resulting in migration from low to high flow regions, with the high flow vessel segments stabilising as a result [5]. The polarisation sensitivity with regards to flow has been shown to be affected by PAR3 [13] and is managed through paracrine Wnt ligand signalling [8]. Wnt signaling can be responsible for lowering the thresholds at which ECs respond to flow, potentially resulting in premature pruning. Likewise pruning can be premature when imbalances occur between Notch and Wnt/ β -catenin signaling events [14]. Beyond Wnt, flow responses are managed by the genes *Klf2*, *Klf4* and *Ptgs2*, adapting their transcription based on flow [15]. Furthermore VE-cadherin, VEGFR2 and PECAM1 are sensing and relaying shear forces [16]. Also, mechanosensitive transcription factors as YAP translocate the nucleus in order to polarise the cell, promoting further transcription of genes related to migration and proliferation [17]. Beyond polarization vascular patterning is also largely influenced by cellular contractility, through e.g. actomyosin contractility as regulated by PI3K [18].

Endothelial cell migration, which involves the steps of extension at the leading edge, adhesion to the matrix and release of adhesions at the rear, is steered by three major mechanisms, namely chemotaxis, haptotaxis and mechanotaxis. As for chemotaxis, the primitive plexus is formed under influence of VEGF, which promotes the migration of ECs such that, along with cellular elongation, blood islands will fuse and form tubular structures in the process of establishing the primitive vascular plexus [19], [20]. Merks et al. have shown that steric hindrance suffices for network formation, yet networks develop more rapidly with chemotaxis [21].

The current understanding of EC migration up the flow gradient in the process of vascular stabilisation [19] highlights primarily the role of mechanotaxis, the directional migration generated by mechanical forces. The protective layer of glycocalyx and embedded glycoproteins on the luminal membrane transmit hereby, via signaling to the cytoskeleton, shear stress forces to integrins and cell-cell adhesion components [19]. The shear stress forces are further transmitted such that they activate a signaling pathway inside the cytoplasm that contribute to microtubule elongation, followed by Rac activation and, in turn, actin polymerization which leads to lamellipodia protruding in the flow direction [19]. The Golgi complex is hereby positioned through microtubule-linked motors [22] which has assisted researchers in establishing the migrational direction of ECs [23]. In addition to signaling pathways that trigger polarized endothelial cell migration there are also responses that involve dissociation of cell-cell contacts. It is presumed that these shear stress forces regulate EC migration more than chemotaxis does in large vessels, due to the strong convectional forces in these high flow vessels. This is despite the observation that the force exerted by shear stress, if uniformly applied over the entire endothelial surface, is roughly 1000 to 5000 times weaker than traction forces of focal adhesions [24]. The onset of shear stress has been shown through in vitro research to decrease tension across VE-cadherin, paralleled by a lower total cell-cell junctional tension [25]. This decrease in total cell-cell junctional tension incites towards cellular motility. Beyond mechanosensitive migration endothelial cells can perform chemotactic migration. This involves the breaking down of cell-cell adhesions, VEGF stimulates this by dissociating the VE-cadherin/ β -catenin complex at adherens junctions [19]. The chemotactic strength has been shown to be dependent of molecular factors, important examples of which are NO and ROS [19]. NO, produced by eNOS after activation by VEGF, plays a role as major regulator of cell migration. Inhibition of NO production has been

shown to block the chemotactic action of VEGF. It is presumed to modulate angiogenesis through inducing a vasodilation-associated expansion of the endothelial surface such that a more optimal response is evoked towards angiogenic and promigratory agents. ROS is a signaling molecule that might influence the chemotactic response as it is involved in VEGF-induced autophosphorylation of VEGFR-2.

Dejana has shown that the effects of VEGF are context dependent, where VE-cadherin makes it such that ECs only sense VEGF at the EC-ECM border, such that inner positioned ECs stabilise and freely positioned ECs are incited towards movement. Knockouts of VE-cadherin can potentially lead to blood islands with knockouts of the causal VE-cadherin [26]. Interestingly, at lower motility ECs are inclined to aggregate and become compact in shape, in contrast to high motility which links with many pseudopod extensions. The retractive component of chemotaxis, which occurs when peripherally positioned cells invade inwards and displace the inner cells in their migration up the VEGF gradient, promotes sprouting behaviour even at lower motilities [27].

With respect to rheology, the shear stress relates to the velocity loss that occurs due to friction of the blood with the endothelial cells that make up the vascular inner lining. Another crucial component is the Hagen-Poiseuille equation, which outlines the relationships between fluidic pressure difference, volume flow rate and vascular resistance. Poiseuille's law assumes conditions at which flow is laminar, partly explained by a low Reynolds number. In arterioles and capillaries the Reynolds numbers, the ratio of inertial to viscous forces, have been measured in human subjects as 0.5 and 0.002 respectively [28] and in this respect Poiseuille's law is better fit for modeling of the capillaries than arterioles. Partly, the lowered Reynolds number is due to the lowered average velocity in blood in the capillaries, 0.001, as opposed to 0.05 in the arteries [28]. This velocity drop can be explained by means of Poiseuille's law which states that the volumetric flow rate over a vessel is proportional to the fourth power of the vessel radius.

Conceptual models

The Anderson-Chaplain model [29] is a well-known model in studying angiogenesis. Its primary aims are to investigate how chemotaxis and haptotaxis affect the migration of endothelial cells and the influence of EC proliferation on the capillary network formation. The model has shown morphological similarity to capillary network structures observed in vivo. Despite its usefulness in investigating the spatiotemporal evolution of the vascular network, the network is in a continuous explorative phase of sprouting and does not undergo remodelling events. Vessel regression is, however, an important aspect in stabilisation of the primitive vascular plexus and rules for such a regression event would have to be described explicitly in the descriptive Anderson-Chaplain model. When implementing variable flow the model would also require its vessel segments to be variable in cross section size. These rules would then have to be encoded explicitly, in addition to rules that specify tip cell motility, branching and anastomosis events. In addition it states assumptions with regards to vessel length. Interesting correlational results could then be obtained from correlating e.g. vessel regression with either flow shear stress or pressure and validate the results for the closest match against in vivo data. However, the descriptive rules that give rise to remodelling events would exempt us from investigating causal underlying molecular or cellular mechanisms that could induce stabilisation of the primitive plexus. Cell-centred approaches, such as those highlighted by Merks and Glazier [30] are well suited to model vascular explorative and remodelling events. Where specifically for this research the cell-based in silico model of vasculogenesis, with application of chemotaxis, by Merks et al. [21] is of relevance as it provides us with the mathematical model which allows us to set up the structure of the primitive vascular plexus upon which the flow-based angiogenic remodelling events can be simulated. The described cell-based models make use of the lattice-based Cellular Potts Model [31] (CPM), which simulates individual and collective cell behaviour with dynamics governed by a single energy function. It is necessary to define parameters and subcomponents of this energy function, yet from local decisions which are made on the basis of this Hamiltonian energy function behaviours such as sprouting and regression events arise. ECs show morphological variation as their membrane can either protrude or retract, a choice made by assessing the cells chemical, mechanical and morphological state and feeding them into the energy function. Communication is also well modelled through extensions of the energy function, with cells (the in silico representation of ECs) and medium (extracellular matrix) able to secrete or uptake chemicals and affect neighbours through their morphology or mechanical influences. Collective behaviours arise from these local interactions. Since behavioural decisions are based on an unifying energy equation, which does not require tuning for different behaviours such as sprouting or regressing, the model lend itself well to investigate the

underlying chemical and/or mechanical principles that steer remodelling of the vasculature towards stabilisation. In contrast to the Anderson-Chaplain model in which rules were described on the vessel segment level, the cell-based model define rules on the chemical and molecular level. This frees us to investigate how the events on the molecular scale affect the structural changes that occur on the cellular scale.

Despite the spatiotemporal accuracy of these models with respect to in vivo observations, the work excludes haemodynamics. Bernabeu et al. [12] have created a three-dimensional capillary network model in which flow was simulated using a computational fluid stimulating method called the Lattice Boltzmann algorithm. The construction of their geometrical model was based on experimental image data. Constructing models at different timestamps, calculating flow-related forces for each model and observing structural changes between models allows for correlating haemodynamics with structural remodelling events.

Whereas the model from Bernabeu et al. was constructed based on sample images from experimental data, Gödde and Kurz [9] constructed a dynamic model in which structural remodelling was based on haemodynamics and other extravascular properties. Their model made use of feedback loops in which haemodynamic forces were recalculated after any structural change, with these forces in turn influencing further stochastic sprouting or remodelling events. A similar approach was used by Welter and Rieger [10]. Both models simulated haemodynamics, with structural changes through attachment of tripod vessel structures or degeneration of individual vessels. This scale is, however, too coarse for making predictive statements on the molecular or cellular scale, such as the possible influence of cellular adhesion molecules or cellular contractility on remodelling events. In addition, new sprouts are limited to a small set of possible directional angles in which to protrude. More importantly, addition, growth and degeneration are managed through separate function which prevents us from uncovering unifying causal principles.

Objective and expected results

We strive to uncover how flow dynamics can stabilise the vascular network as set up during the process of vasculogenesis, such that a vascular tree results in a differentiable hierarchy in vessel thickness and therefore rate of fluid flow.

In the previous sections we highlighted research which showed that (a) the vascular network stabilises through flow [4] [9], (b) ECs migrate up the flow gradient through WSS sensing [5][19], (c) glycocalyx and embedded glycoproteins on the luminal membrane [19], as well as VE-cadherin, VEGFR2 and PECAM1 [16] are sensing and relaying shear forces, (d) chemotactic sensing can be modulated through molecules as NO and ROS [19].

VEGF can be secreted by cells that are hypoxic [32]. In our research we assume that VEGF is, in addition to being sensed by ECs, also secreted by the cells such that they attract each other, in lines of the work by Ambrosi et al. [33]. Biologically, we assume that WSS could make the cells less sensitive towards chemical signalling molecules through coupling of a WSS sensing complex (c) with a modulator of chemotaxis sensitivity (d).

We put forward the hypothesis that flow might inhibit the sensitivity of endothelial cells with respect to the chemoattractant VEGF. This hypothesis is tested for by researching if the flow-based inhibition mechanism can result in cellular migration up the flow gradient (b) resulting in vascular stabilisation through a differentiable hierarchy in vessel volume and quiescence of cells in high flow vessels (a).

The suggested mechanism is as follows: small perturbations in vessel thickness give rise to variation in volume flowrate and therefore WSS. Thicker, high-flow segments will repress cell motility through flow-based chemotaxis inhibition and therefore give rise to the accumulation of ECs, which in turn expands the vessels more through a positive feedback loop. The feedback loop is expected to halt when the rates of ECs regressing into the high-flow segments slows down as neighbouring vessels get progressively thinner, and the rate of outgoing ECs increases due to a rising concentration of cells in the high-flow segment.

To investigate the hypothesis, we need a conceptual model. The analysis of which has highlighted the following requirements: (a) the model should perform structural changes on a cellular scale such that signaling methods between neighbouring cells can be taken into account, (b) the model should implement an approach to remodelling in which unifying and integrative rules give rise to both generative or degenerative remodelling, (c) the model should have potential to show variation in flow through adaptive vessel thickness, as a result of the unifying rules, (d) the flow dynamics and structural remodelling should be coupled through a feedback mechanism.

With respect to these conditions, we desire to create a model that allows for investigation into principal components that can mediate vascular stabilisation through flow dynamics. The cell-based CPM adheres to all conditions. To simulate the angiogenic remodelling of the primitive vascular plexus as established through vasculogenesis we will base our work on the vasculogenesis simulating CPM model from Merks et al. [21]. Yet, the application of blood flow dynamics on the CPM model has to our knowledge not yet been attempted. The objective arises to expand the cell-based CPM model with haemodynamics, which will provide us with the conceptual model for our analysis.

First, the report describes the method of flow extraction, which we strive to solve through a computationally efficient manner. Next, the methods for flow-induced chemotaxis repression will be outlined. Lastly, results from the haemodynamic extraction and flow-based chemotaxis inhibition will be analysed. Followed by discussion.

2 Method

2.1 Approach

Our mathematical model is based on the two-dimensional CPM model of vasculogenesis by Merks et al. [21] in which our work focusses on angiogenic, functional remodelling such that a vascular tree can be established. We constrain functional remodelling to remodelling events driven by haemodynamic influences. The framework for implementation is the Tissue Simulation Toolkit [34], as it is designed for cell-based CPM simulations of vascular morphogenesis and lends itself well for experimentation with alternative model design choices. The Cellular Potts Model will set up the structure of the angiogenesis model. Each simulation step consist of a Monte Carlo Step (MCS), which entails an asynchronous iteration over the entire lattice where n copies are attempted, with n the number of lattice sites. These copies simulate stochastic membrane fluctuations which extend or retract the endothelial cells in interactions with the extracellular matrix (cells and medium in the context of the CPM).

We attempt copies by iterating asynchronously over all lattice site pairs (\vec{x}, \vec{x}') found on cell-cell and cell-medium borders. For each, the Hamiltonian H (eq. 1) needs to be calculated before such an attempt is made as chemoattractant concentrations, adhesion preferences between cells themselves and between cells and medium, target area and length deviations lead to behaviour by means of their influence on the effective energy.

$$H = \sum_{\vec{x}, \vec{x}'} J(\tau(\sigma_{\vec{x}}), \tau(\sigma_{\vec{x}'})) (1 - \delta(\sigma_{\vec{x}}, \sigma_{\vec{x}'})) + \lambda_1 \sum_{\sigma} (a_{\sigma} - A_{\sigma})^2 + \lambda_2 \sum_{\sigma} (l_{\sigma} - L_{\sigma})^2 + \chi(C_{\vec{x}} - C_{\vec{x}'}) \quad (1)$$

Central to the CPM is the calculation of adhesion energy between two cells. This adhesion energy influences the preference of the cellular membrane to either extend or retract, dependent on whether the state before or after such an action is favourable. Between all lattice site pairs $(\sum_{\vec{x}, \vec{x}'})$ where the spins $\sigma_{\vec{x}'} \in [0, n]$ are of different types $(1 - \delta(\sigma_{\vec{x}}, \sigma_{\vec{x}'}))$, with δ the Kronecker delta. Adhesion strength is calculated through a formula (J) that takes as input the types of the neighbouring cells $(\tau(\sigma_{\vec{x}}), \tau(\sigma_{\vec{x}'}))$. A lower J value is indicative for tighter contact between cell membranes. The result of the summation provides the total energy of that system, the Hamiltonian H . The system desires to change into a lower energy state. The computations are solvable locally. A random lattice site \vec{x} is chosen with an adjacent lattice site \vec{x}' , where the index $\sigma_{\vec{x}'}$, is replaced by the index of \vec{x} , in the context of membrane extension or retraction, when the change in total effective energy that would occur if the copy were to be made is negative. Else, dependent on the Boltzmann temperature T which scales exponential with the amount of noise in the system, the move will still be made with a probability of $e^{-\Delta H/T}$.

Notably, the CPM has an area constraint $(\sum_{\sigma} (a_{\sigma} - A_{\sigma})^2)$ which strives to push the area of each cell to a target volume (375 lattice sites). the strength of which depends on the Lagrange multiplier λ_1 (50) that simulates cell elasticity. Merks et al. showed that cell elongation plays an important role in angiogenesis [21], as such simulations of this kind are enhanced in the likes of the mentioned research by incorporating a length constraint in the Hamiltonian, where v and V are replaced by corresponding l and L (125), with the effect influenced by a separate Lagrange multiplier of equal strength. The authors have shown that this replicates stable in vitro vascular network growth and as such their adaptation of the CPM provides the basis of our model.

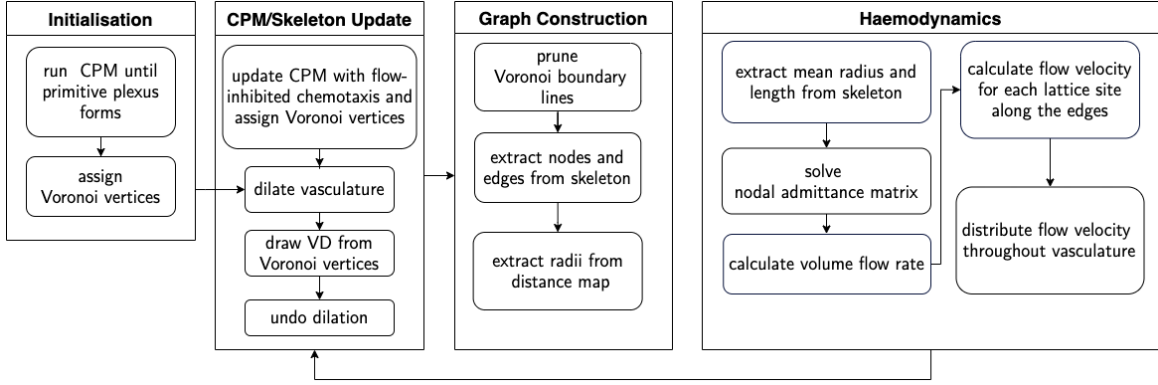


Figure 1. Overview of the simulation algorithm. The CPM runs until formation of a primitive network, at which point Voronoi vertices are assigned to any lattice sites of type medium that have at least one lattice site of type cell as neighbour. Next, the simulation loop is run in which CPM and skeleton updates are followed by graph construction and haemodynamic extraction, for which the flow velocity extracted from the latter will be fed back into the algorithm for flow-inhibited chemotaxis.

An initial blob of 100 cells of size 32 is simulated for 30 MCSs, after which the CPM starts interacting with the PDE.

The PDE (eq. 2), used by Merks et al. [21], is based on the assumption that endothelial cells secrete the chemoattractant which is degraded by the ECM [33], as such the implementation includes the the chemoattractant secretion rate α ($2.5 \times 10^{-3} \text{ s}^{-1}$) and the decay rate ε ($1.8 \times 10^{-4} \text{ s}^{-1}$). D ($1.8 \times 10^{-13} \text{ m}^2 \text{ s}^{-1}$) specifies the diffusion coefficient.

$$\frac{\delta(c(\vec{x}, t))}{\delta t} = \alpha \delta(\tau(\sigma \vec{x}), \text{cell}) - \varepsilon(\tau(\sigma \vec{x}), \text{medium}) C_{\vec{x}} + D^2 C_{\vec{x}} \quad (2)$$

The PDE calculations in which VEGF concentrations are diffused are made on a layer where the lattice matches the CPM lattice, using 15 diffusion steps per MCS with time step of the finite-difference integrator, Δt , set to two seconds and Δx , the size of the pixels for the integrator, $1.8 \times 10^{-4} \mu\text{m}$.

The cells are motivated to extend their filopodia in the direction of chemoattractant gradient [35], as this brings about a negative change in effective energy at the time of copying [36], see equation eq. 4. The parameter χ defines the strength of the chemotactic component. Chemotaxis sensing is in our model inhibited by flow velocity, see equation, 3, for which we have defined ζ (m s^{-1}) which equals the velocity when chemotaxis sensing will be completely deactivated. To have cells sense VEGF throughout their membrane, instead of only at cell medium borders, we turn off contact inhibition such that cells in the inner parts of the vasculature are not exempted from obtaining a flow-dependent quiescent state. The extraction of the velocity component is explained in Section 2.5.

$$\chi' = (1 - \min(1, v_i/\zeta)) * \chi \quad (3)$$

$$\Delta H' = \Delta H - \chi' \delta(\tau(\sigma \vec{x}), \text{cell})(C_{\vec{x}'} - C_{\vec{x}}) \quad (4)$$

After MCS 100 a primitive form of the vasculature has arisen and various computational processes follow, highlighted in the diagram of Figure 1, with the final goal for each simulation step to extract haemodynamics based on the vascular structure such that flow-inhibited chemotaxis can be modelled. The Hagen-Poiseuille equation (eq. 5) allows one to calculate the pressure difference between two ends based upon the length of a vessel, volume flow rate, π , vessel radius and the viscosity, motivated further in Section 2.5. With viscosity being influenced by various factors, for our purposes it can be set as the constant 1.

$$\Delta p = \frac{8\mu L Q}{\pi r^4} \quad (5)$$

To derive the radius and length variables, further defined in Section 2.2, the vasculature is made binary where the foreground is defined by $\{\vec{x} | \delta(\tau(\sigma \vec{x}), \text{cell})\}$. Application of the generalized Voronoi diagram method, where Voronoi vertices are placed along the vascular contour, generates regions of influence (eq. 6) for each vertex. Only where regions meet are boundary lines drawn,

where all are pruned except those found in the midline of the vessels such that the desired skeleton arises.

After skeletonisation a graphical structure is derived with edges (i, j) over the nodes $i, j \in V$. Where $0 < |\{(i, j)\}| < \binom{n}{2}$, $n = |v|$, $(i, j) \in G$ and $i, j \in V$. Through actively applying the processes as described in Section 2.2 the network will hold information concerning edge length, one value per edge, and radii, many values per edge. We derive flow conductivity per vessel, G_{ij} , through Poiseuille's law from \bar{r}_{ij} (lattice sites) and L_{ij} (lattice sites). The unknown values are now capped to pressure and volume flowrate. Conditions hold for volume flowrate, which is zero when one localizes on the nodes, where the fluidic inflow equals the outflow. Boundary conditions are provided by simulation of a tissue engineering environment with flow in- and outlets, where we can place nodes at the sprout ends whenever they tap into the the boundary of the simulated tissue engineering environment. Which they are motivated to do as the adhesion energy between ECs and the simulated walls, with pressure maximal and minimal at the vertical boundaries, with interpolated values horizontally. The Hagen-Poiseuille equation shows that all input values now have been derived for each edge segment, the pressure on the head and tail node can now be calculated by solving the nodal admittance matrix to get \vec{p} . At this stage volume flowrate is only known locally and not over the edges, thus we calculate the volumetric flow rate Q over the edges (i, j) with $Q_{ij} = G_{ij}(p_j - p_i)$. Finally, the velocity is derived from the volumetric flow rate and made accessible to the cells such that flow-inhibited chemotaxis can be simulated in order to decrease motility in high flow segments in the hopes of stabilising them through a positive feedback loop of relative high flow, thickening of the vessels and further increasing flow as Poiseuille's law states that it scales to the fourth power of the radius.

2.2 Graph Construction

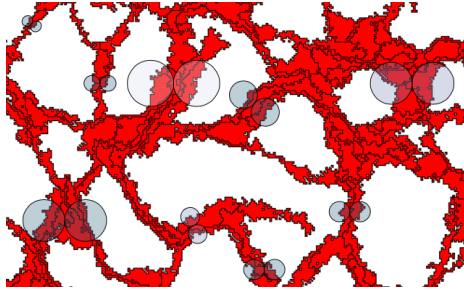


Figure 2. The radius at each voronoi vertex is calculated from the maximum inscribed circle. Extracting radii from vessel segments can be conceptualized by imagining the incremental inflation of circles until the paired circles touch, with the circles positioned on both sides of the enclosing walls at given loci. When the pair of circles are inflated by a boundary layer of size 1 during each computational inflation step they should be of equal size when the pair touches or overlaps, with their radius equal to the inner radius of the vessel cavity (or roughly equal, in the case of an uneven distance between opposing walls). Note at the lower right corner that redundant midlines can be drawn that will require pruning at a later stage, see section 2.4.

To extract radii from binary vessel segments one could posit circles along the vascular contour and increment their radii until the paired shapes touch, see Figure 2.

Difficulties arise due to it being unclear where to place these inflating shapes. This can be circumvented when the vessel walls are broken up into discrete parts and one such shape is placed at each wall segment. Next, replace circles with objects that hold no constrictions on their shape and dilate these shapes simultaneously with an added layer of one point in thickness until neighbouring regions touch. The process is equivalent to the construction of a Voronoi diagram (VD), its gradual construction visualised in Figure 3.

The aforementioned operations ask for mathematical notation. Voronoi vertices $P_{\vec{x}}$ are positioned on the Voronoi layer, of equal dimension as the CPM/PDE layer, at lattice sites of type medium with a lattice site of type cell in its Moore neighborhood, such that the cells belong to the set $\{\vec{x} \mid \delta(\tau(\sigma_{\vec{x}}), \text{medium}), \delta(\tau(\sigma_{\vec{x}'}), \text{cell}), \vec{x}' \in \text{Moore}(\vec{x})\}$. $P_{\vec{x}}$ is associated to region $R_{\vec{x}}$ (see equation 6, with $d(a, b) = \|a, b\|$), which consists of the set of cells for which each associated cell \vec{x}'' has no other voronoi vertex $P_{\vec{x}'}$ within closer distance. Regions are only defined on the foreground $\{\vec{x} \mid \tau(\sigma_{\vec{x}}) = \text{cell}\}$.

$$R_{\vec{x}} = \{\vec{x}'' \mid d(\vec{x}'' - P_{\vec{x}}) \leq d(\vec{x}'' - P_{\vec{x}'}), \forall P_{\vec{x}'} \neq P_{\vec{x}}, \delta(\tau(\sigma_{\vec{x}''}), \text{cell}), \delta(\tau(\sigma_{\vec{x}}), \text{medium})\} \quad (6)$$

Disconnected Voronoi vertices can with simple modifications, such as the assignment of a minimum distance between two Voronoi vertices before its inner boundary line is drawn, positioned such that they form shapes, at which point we refer to the generalized Voronoi diagram. See Figure 4 on how the shape made by the connected vertices can overlay the vascular contour. In our project a Voronoi boundary line is only drawn at a lattice site when it has a squared euclidean distance greater than two (in units of pixels), not adhering to this condition would greatly increase the number of boundary lines drawn as any roughness in the vascular contour could elicit a boundary line being drawn in a concave part of the vascular wall.

We name the collection of the connected Voronoi boundary lines the skeleton.

The midline of the vasculature can be derived from the skeletonised shape when only those parts remain when the regions that border the Voronoi boundary lines are associated to vertices that overlay opposing vascular walls, with the necessary pruning of boundary lines further explained in Section 2.4. The euclidean distance from the midline to the instantiating Voronoi vertices can then be used as a proxy for the radius.

Concretely, the region $R_{\vec{x}}$ associated to Voronoi vertex $P_{\vec{x}}$ continues to expand until assigning lattice sites of neighbouring region $R_{\vec{y}}$ to $R_{\vec{x}}$ would violate condition 6. At which point a Voronoi boundary line is positioned either at lattice site \vec{x} , from which the radius $\frac{1}{2}(d_{xx} + d_{xy})$ will be extracted when iterating over the Voronoi boundary lines at a later processing stage, or site \vec{y} , with:

- $d_{xx} = \|\vec{x} - P_{\vec{x}}\|$, $d_{xy} = \|\vec{x} - P_{\vec{y}}\|$
- $d_{yy} = \|\vec{y} - P_{\vec{x}}\|$, $d_{yx} = \|\vec{y} - P_{\vec{y}}\|$.

The selection is made by the choice which least violates the condition that the distance from a Voronoi lattice site to its associated Voronoi Vertex should equal the distance from the site to the Voronoi Vertex associated to the region which made the algorithm halt.

For example, lattice site \vec{x} is skeletonised, as opposed to \vec{y} , when the absolute difference between d_{xx} and d_{xy} is lower than that between d_{yy} and d_{yx} .

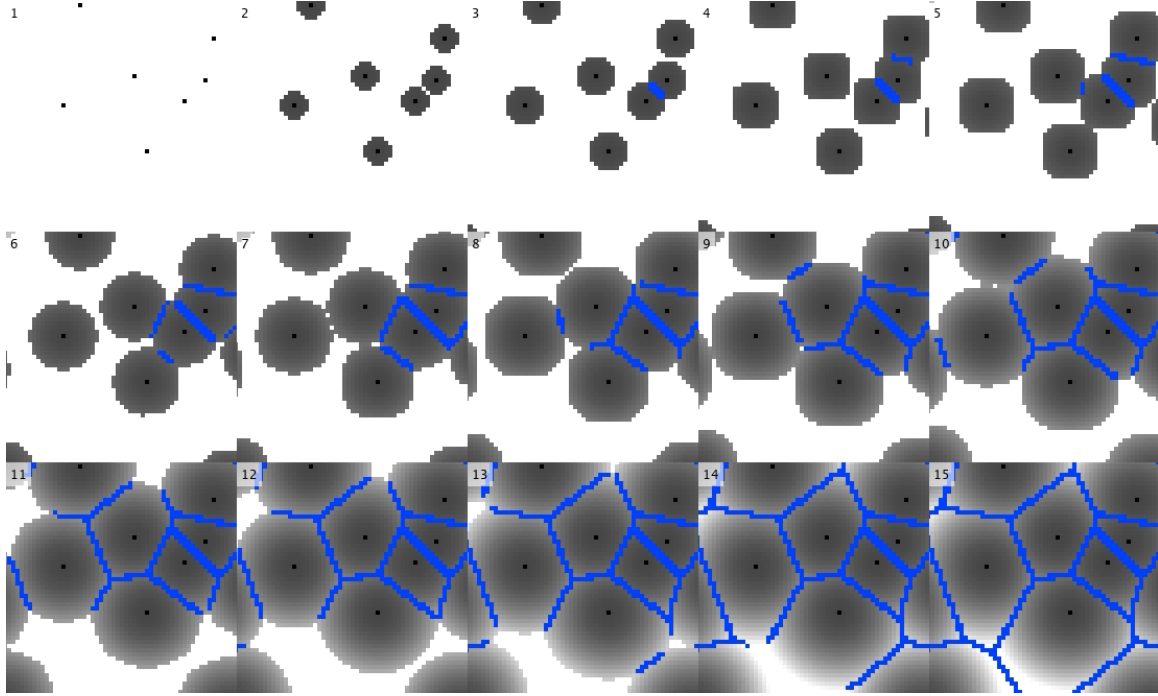


Figure 3. Voronoi diagram construction through incremental dilation. One approach to construct a Voronoi diagram is by extending regions associated to vertices through incremental dilations performed simultaneously from all Voronoi vertices, as neighbouring sites are queued (each site expanded into queues its neighbours) and dequeued with distance priority. Distance queueing is possible as each site knows, by means of a continuously updating distance map, to which region and therefore vertex it belongs, along with the distance from site to vertex. Consider the counterfactual where distance queueing is not applied, where first the region of just one Voronoi vertex could continue to expand. To know when to halt, it would need to calculate distances from the site to all Voronoi vertices on the lattice to check if further regional expansion is justified according to equation 6. With incremental, synchronised dilation if we consider whether or not to halt we only need to check if the distance to the current vertex would be lower than the distance to the vertex associated to the region in which the algorithm expands.

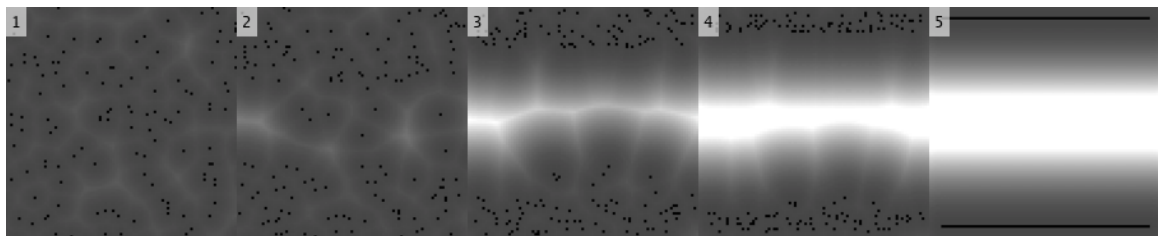
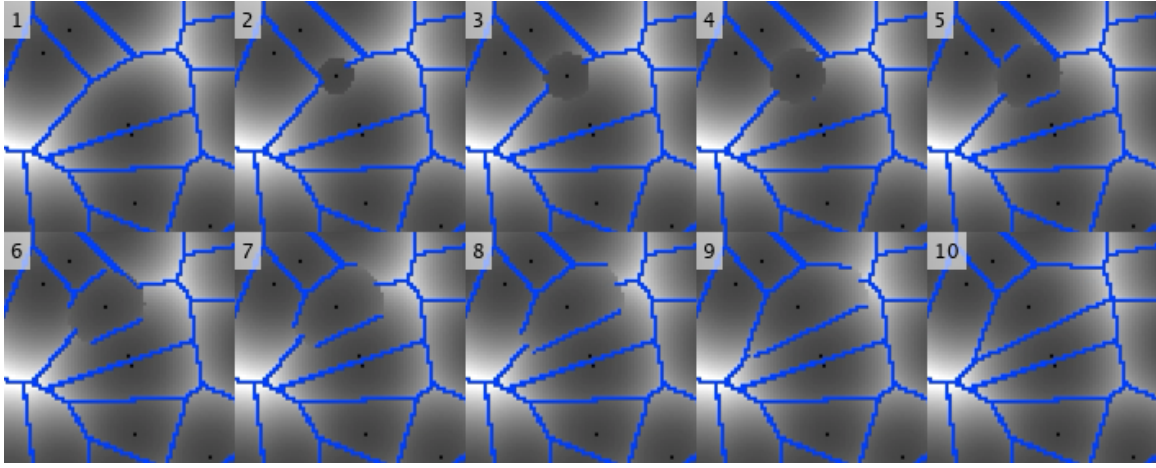


Figure 4. The generalized Voronoi diagram. Connecting the vertices of the Voronoi diagram allows for the construction of shapes.

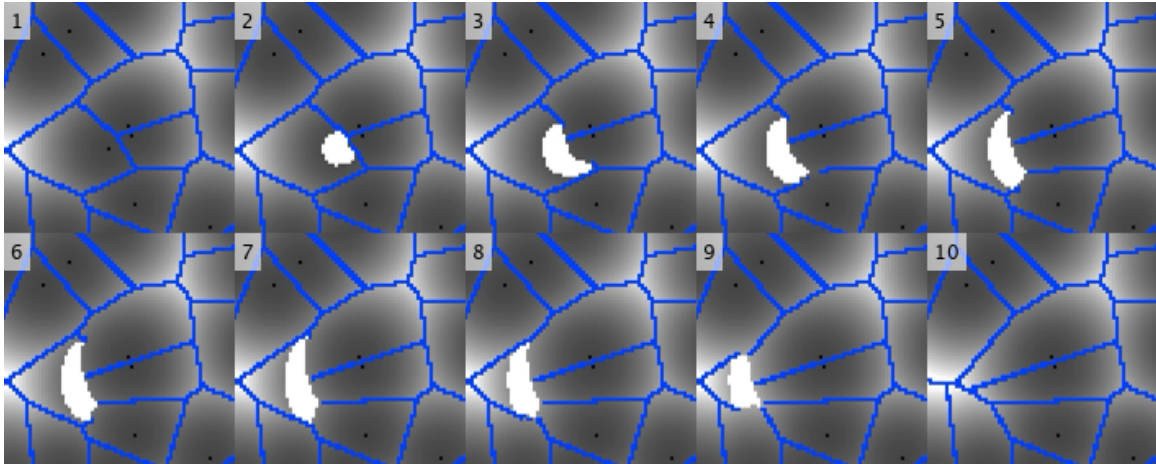
2.3 Dynamic Graph Construction

Dijkstra's algorithm picks an unvisited vertex which holds the lowest distance to the starting vertex and updates distances through it to each unvisited neighbor. Updating the neighbor's distance only if shorter than its previously calculated distance. Visited vertices are marked. Now, the same algorithm can be applied on a lattice, where lattice sites become vertices and edges are virtually drawn between any pair of lattice sites in each others Moore neighbourhood. A priority queue is used for which lattice sites have their dequeue priority inversely related to distance. Lau et al. [37] use this principle in combination with a *lower* and *raise* operation as described in Figure 5. These operations allow for localized updates. This lessens the computational load on the Cellular Potts Model as updates occur only at the boundary between cells and medium.

The algorithm executes a *lower* operation if a Voronoi vertex has been placed. It marches outwards by iterating over the Moore neighborhood of the last dequeued cell, where lattice sites with the smallest distance to the newly positioned vertex are dequeued first and any sites with equal distance are dequeued without preferential order. Lattice sites \vec{y} of the region $R_{\vec{y}}$ are assigned to



A



B

Figure 5. Localised updates of the Voronoi diagram for dynamic skeletonisation. The lower operation **(A)** is executed after placing of a Voronoi vertex for which all lattice sites are overwritten and made part of its region if this would result in a smaller distance vector, using euclidean distance. Boundary lines are drawn where the algorithm halts. If a Voronoi vertex has been removed **(B)** all lattice sites belonging to its region are updated with values of infinity during the raise operation such that they will eventually be overwritten through the "smaller than" condition associated to the lower operation, which are initiated from any of the regional bordering Voronoi lattice sites.

$R_{\vec{x}}$ and queued with distance priority if $\|\vec{y} - P_{\vec{x}}\| < \|\vec{y} - P_{\vec{y}}\|$. If not, the algorithm halts and posits a boundary layer. The distance $\|\vec{y} - P_{\vec{x}}\|$ is stored in \vec{y} such that the radius can be extracted if \vec{y} will be part of the final skeleton.

Upon removal of a site $P_{\vec{x}}$ a *raise* action resets the associated region into a queued state through Moore neighborhood traversal and overrides the original distance value $\|\vec{x} - P_{\vec{x}}\|$ with a maximal value. When the algorithm propagates itself into a region $R_{\vec{y}}$ it shifts from an outward motion into an inward motion, transitioning from mode *raise* to *lower*, and potentially updates distances to $\|\vec{x} - P_{\vec{y}}\|$ if the "smaller than" condition is adhered to.

2.4 Adjustments

Application of the Voronoi skeletonisation algorithm results in many redundant skeleton segments. Lau et al. [37] prune these away by placing walkers on the extremities of the thinned shape and walking them inwards whilst they prune the path, until arriving at a crossing. An Y shape would be completely pruned away even if one would only posit the walkers at the upper two ends, as one walker would stop at the first crossing, after which a second walker would prune away the top V and continue walking down until the shape is completely pruned away. The shape $-O-$ would result in O . We will simulate a tissue engineering environment in which fluid will flow in and out through the tissue engineering environment margins. For this to occur it is necessary to preserve the skeletonised lines when they attach to the margins. The result of the preceding steps is a pruning of all extremities with only those lines remaining that are connected to the flow in- and outlet simulating walls of the tissue engineering environment.

Further required adjustments are the removal of spurious loops and disconnected skeleton fragments which can occur at small passages. It would be possible to let the skeleton pass through even the smallest bottlenecks by smoothing restrictions on the placement of Voronoi boundary lines. For example, by placing Voronoi boundary lines in between two Voronoi vertices separated by only two lattice sites. However, this would lead to an increase in unconnected ends and place undue demands on the pruning algorithm. A preferable approach would be to dilate the vasculature. Which is done by performing a synchronous MCS and toggling the type of the lattice sites from type medium to cell if they have at least $\psi \in \mathbb{N}$ adjacent neighbours of type cell. In mathematical description, all lattice sites belonging to the set $\{\vec{x} \mid |\{\vec{x}' \mid \delta(\tau(\sigma'_{\vec{x}}), cell), \vec{x}' \in nbs(\vec{x})\}| \geq \psi, \delta(\tau(\sigma_{\vec{x}}), medium)\}$, where the function nbs retrieves the Von Neumann neighborhood and ψ is inversely coupled to the aggressiveness of the dilation, set in our model to 1 for maximal dilation. To fill larger holes, the dilation step can optionally be repeated for a given number of times. Dilation has the additional desired effect of removing unwarranted cycles. The computation does however place demands on computation time and slightly alters the radii distribution as small vessels are in greater proportion affected by dilation than large vessels.

The thinned shape is now transformed into a network. Since each vessel cell holds information about the distance to its closest wall the radii can be read out from cells that are part of the pruned skeleton. The resulting graph has nodes with associated edges, with each edge storing a number of radius values equal to its length in grid cells. At this point final adjustments are made to remove any looping edges from the network that have escaped the pruning algorithm.

The vessel segments are further split in smaller sections for increased accuracy. That is, the pressure distribution over a single vessel segment between two nodes with radii $\{10, 8, 12, 9, 4, 2, 4, 5\}$ is further divided in parts, such that haemodynamics are separately calculated for the segments with e.g. radii $\{10, 8, 12, 12\}$ and $\{9, 4, 2, 4, 5\}$ where decreasing the sampled radii aims to minimise $SD(\bar{R})$ and minimise the violation of the Hagen-Poiseuille constraint of constant cross section over the vessel.

2.5 Haemodynamics

Kirchhoff's circuit law states: "The algebraic sum of currents in a network of conductors meeting at a point is zero". Now, analogies can be drawn between electricity and fluid flow making these laws directly applicable to the fluid domain. The fluidic equivalent of Ohm's law, $V = RI$, is the Hagen-Poiseuille equation (5).

A subcomponent of this equation is resistance (eq. 7), the impeding effect exerted by materials upon one another. Fluidic resistance has, like electric resistance, the property of being proportional to the length transporting segments and is affected by the radius. In the forementioned fluidic equation conductivity scales by the inner radius of the vessel cavity to the fourth power, implying a relatively drastic increase in conductivity for a widening of a vessel. A remaining component is the viscosity of blood μ , which we set as a simplification to a constant.

The pressure difference between two nodes connected by a fluid vessel is an analogue of electric potential difference (Voltage). The attributes of fluidic conductivity and pressure combine into equation 8, with the volume flow rate \mathcal{Q} equal to the fluid volume passing through a cross-sectional area per unit time and Δp_{ij} equal to the pressure at node j minus the pressure at node i . That is, a positive value would be indicative of fluid flowing from node i to j .

$$R = G^{-1} = \frac{8\mu L}{\pi r^4} \quad (7)$$

$$Q_{ij} = G\Delta p \quad (8)$$

$$Q_i = 0, \forall i \in N \quad (9)$$

where Q_i equals $\sum_{j \in E_i} Q_{ij}$, with $i, j \in N, (i, j) \in E$.

The density ought to remain constant for a parcel of fluid moving with the flow velocity. Thereby implying zero divergence, formalized by condition 9 stating that the summation of the outgoing volume flowrate should always equals zero. In other words, the incompressibility of the flow is maintained when the inflow at any node equals the outflow.

G_{ij} is known for all edges (ij) and filled in for matrix A , row i , column j . μ and π are constants and the radius and vessel lengths are calculatable as described in Methods. Values of which are set in the nodal admittance matrix. What remains is to extract the pressure over the nodes by means of the following formula, with Q as the vector of all Q_i :

$$A\vec{p} = Q = \vec{0}$$

When adapting the matrix equation for boundary conditions, provided by simulated flow in- and outlets of the simulated tissue engineering environment walls, we set \vec{rhs} equal to the zero vector and bring known pressure values over to the right-hand side: $A'\vec{p} = \vec{rhs}$. An example of how to construct the nodal admittance matrix using a minimal fluidic network is shown in Appendix A. To extract p multiply matrix A and vector \vec{rhs} with A'^{-1} . Multiplying a matrix with its inverse results by definition into the identity matrix. See the example below for an implementation of the described process on a network consisting of one input node (red) representing flow input, one output node (blue) and two connecting nodes. The derived pressure can in turn be fed back into equation 8 to get the volume flow rate over the vessel segments.

Flow velocity can be calculated from the volume flow rate through differentiating the volumetric flow over the vessel cross section, under the boundary condition that the velocity decreases to zero as it approaches the vessel wall. However, velocity is in this report approximated by dividing flow volume with the cross-sectional area.

As a following step, we strive to extract flow velocity. Flow velocity is dependent on the vessel radius, which varies throughout a vessel segment. As such, vessel segments are sliced up into slices each one gridpoint in length. For each section we get flow velocity by dividing the volumetric flow rate with the sectional radius. Next, the velocity information, currently contained only in the skeleton sites corresponding to the edge, needs to be made available to the cells. Each cell copies the velocity value from its closest positioned skeleton site. Knowing which lies closest is achieved through calculating a distance map, where we assign skeleton sites as Voronoi vertices and halt the VD algorithm after distance map construction. Formally, we calculate $v_{\vec{x}} = Q_{ij}/\pi r_k^2$ for all \vec{x} positioned along the skeleton from which (i, j) has been derived. We distribute $v_{\vec{x}}$ to lattice sites $\vec{x}' \in R_{\vec{x}}$ (for the definition of the region see equation 6).

3 Results

3.1 Overview

The results highlight the results of simulating haemodynamics as pressure distribution, volume flow rate and flow velocity on the modelled vasculature. This vasculature has been simulated using the TST, with necessary adaptations to implement the desired features. To run this code with a minimal number of computational steps requires that the skeleton is dynamically updated, where any skeleton changes are kept localised to the greatest extent possible. First, the efficiency of the dynamic skeleton updates are assessed, after which an analysis follows with respect to the flow inhibited chemotaxis results.

3.2 Efficient Calculation of Haemodynamics

From Figure 6 it can be observed that in the default unadjusted condition the skeleton can lose connectivity at smaller vessel segments. The Voronoi boundary lines are overall positioned properly, yet one missing skeletonised Voronoi lattice site, such as right above the loop shown in subfigure A, can prevent an entire vessel from being skeletonised. Furthermore, we observe sporadic loops that escape the pruning algorithm, as its method specifies the pruning of all but the connected parts, and loops are connected with themselves. A simple method to prevent missing segments in the skeleton at small passages is to dilate the entire vasculature, as performed in subfigure D where the associated region of influence, B, shows preserved skeleton connectivity. Furthermore, small gaps in the vasculature can be filled through erosion of the medium lattice sites, where subfigure B shows the prevention of non-functional loops. Based on this observation we conclude that dilation of the vasculature before skeletonisation has increased connectivity and minimised redundancy in the skeletal network.

Beyond global skeletonisation there have been localised skeleton updates. The skeleton is updated in a dynamic manner such that the surface area of the generalized Voronoi diagram that needs updating is kept to a minimum. Figure 7 shows a sample MCS with dynamic VD updates which required only ~ 0.7 of the computational steps with respect to the brute force skeletonisation update, where the Voronoi diagram was updated over the entire lattice after a MCS in contrast to localised Voronoi diagram updates in the context of CPM lattice site copies. Nonetheless, it is debatable whether these savings are substantial, as the time savings can be easily overseen in light of the complete pipeline of one simulation step, which also includes dilation, CPM copies, graph extraction and solving the nodal admittance method. After skeletonisation the vascular resistance and vessel radii plus length have been calculated on the derived graph and, through application of the nodal admittance matrix, been used to, successfully, derive haemodynamics (Figure 8).

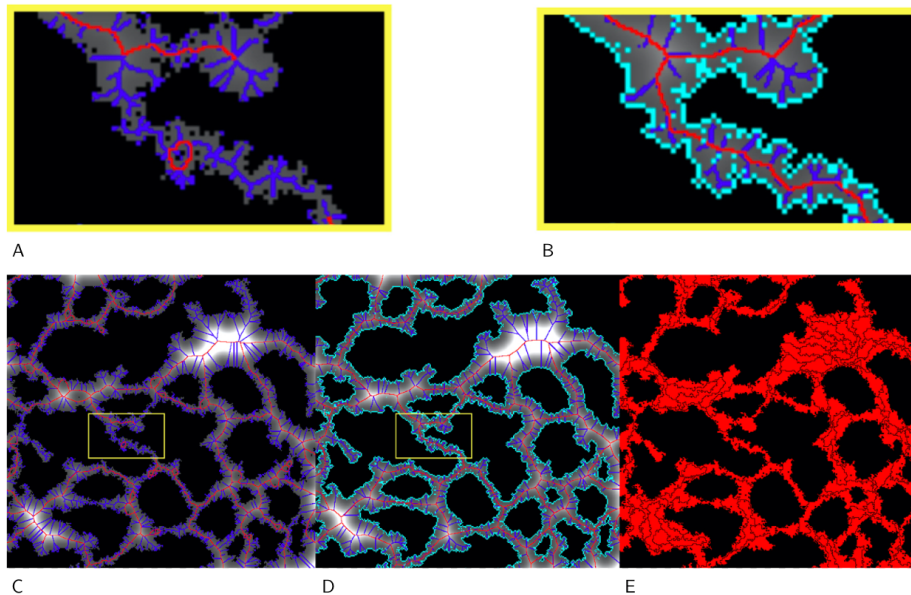


Figure 6. Dilation of the vasculature foreground results in fewer spurious and more connected skeleton fragments. Skeletonisation and graph extraction have been applied in **C**, without dilation, on the TST-simulated CPM model of angiogenesis (**E**). ROI **A** shows solitary loops and unconnected skeleton parts. In **B** we see that these artefacts have been prevented through a preceding dilation of the vasculature foreground before skeletonisation (**D**). The dilations, shown in cyan, replace the medium with cells whenever it has a cell in its Moore neighbourhood. It widens the vasculature, most importantly at passages too narrow for a skeleton to form. Furthermore, the pruning algorithm is tuned to remove any but connected skeleton parts and thereby erroneously skips loops. These loops can, however, be prevented from arising when all gaps in the vasculature are filled through dilation. Taken together, dilation aims to ensure proper connectivity of the skeleton network without superfluous ends. After skeletonisation the dilation steps are undone, else vessels would continuously expand over time.

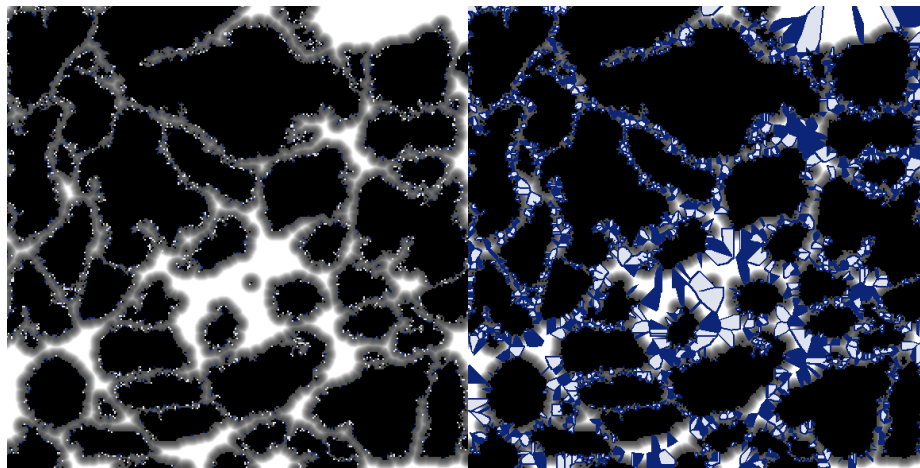
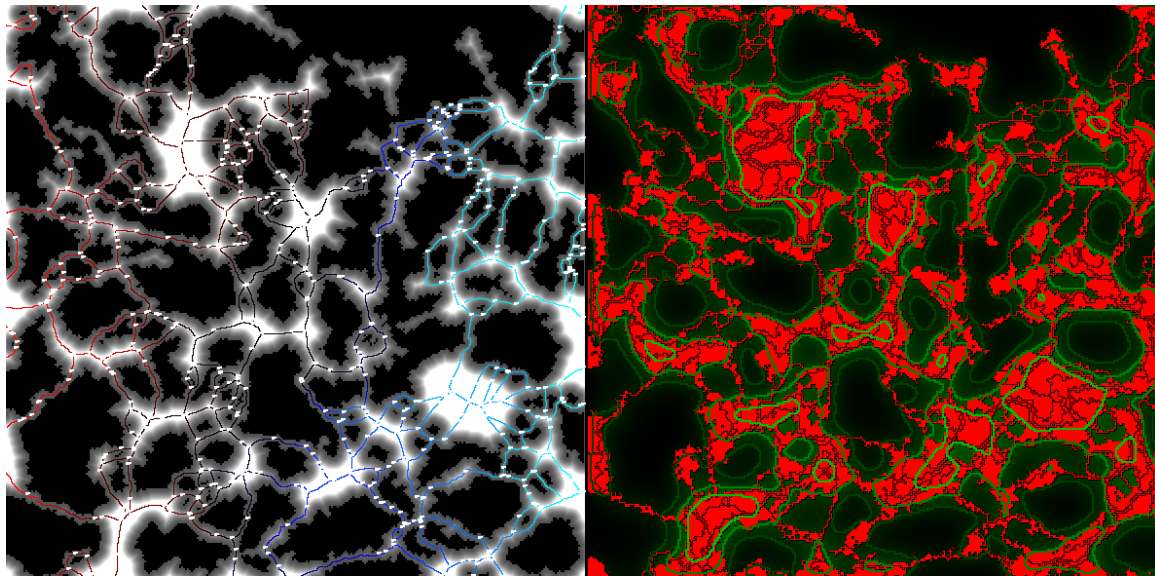
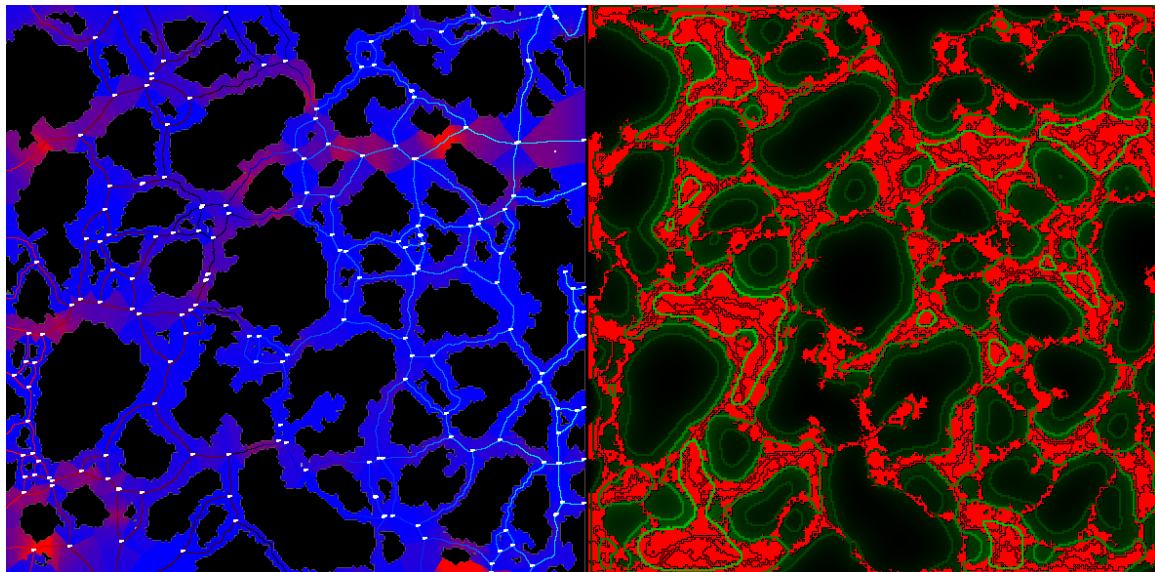


Figure 7. Skeleton updates are only required where its associated region has been affected by CPM copies. The left image visualises lattice site state changes, with the positioning of sites of type cell in blue and medium in grey. The associated regions of the Voronoi diagram that require updating as a consequence are visualised on the right, with lower steps in blue and raise steps in grey (any raise step is eventually followed by a lower step, such that any grey area is indicative of both a lower and raise step). With the trivial update of the skeleton, the entire vasculature would undergo a lower step and the vasculature would thus hypothetically be visualised entirely in blue. At the visualised 200th MCS of the flow-independent configuration 1,564 and 1,559 new lattice sites of type cell and medium were copied into their neighbouring sites. In the dynamic update this resulted in 8,035 raise steps and 255,548 lower steps. The total of 263,583 is, for this sample of VD updates based on local CPM updates, 144% more efficient than the 381,351 brute force steps required for the construction of a VD based on the entire CPM lattice. The efficiency is expected to decrease in steps that show lower average vessel thickness, due to increased motility in the smaller vessels, as the image shows that almost all Voronoi regions in the smaller capillaries are coloured and thus require updating.



A



B

Figure 8. Passages of preferential flow are already visible before the simulation of flow-dependent chemotaxis inhibition. Two random runs at MCS 100, with application of haemodynamics on the simulated primitive plexus, before any significant vascular remodelling has occurred. **(A)** The vascular pressure distribution has been calculated over the graphical representation of the network. The simulated tissue engineering environment provides the in- and outlets with maximal to minimal pressure at left and right boundaries and interpolated pressure values for the upper and lower boundary. **(B)** Flow velocity is shown in red. Initially preferred passages of flow are observable from the vasculature.

3.3 Vascular Stabilisation Through Flow Inhibited Chemotaxis

Figure 7 shows that many copy attempts were made in the smaller vessels, suggesting increased motility. The relative low motility in thicker vessel segments leads us to believe that cells there find themselves in an overall more energetically favoured state. This thus potentially stabilises them. However, stabilising vessel segments could exist as solitary islands that show poor connectivity to other thicker vessel segments. This is unadvantageous as it means that there are no vessels throughout the vasculature which can act as blood flow highways. When the thickening of vessel segments is functional we expect to be able to simulate low resistance, high flow vessels such as the arterioles and venules. When we model flow on a simulated tissue engineering environment, which we have set to show maximal pressure at the left boundary wall into which vessels can tap, minimal pressure at the right boundary wall and interpolated along the horizontal boundaries, the blood will strive to find a passage between the low and high pressure walls of the kit. We expect that any arising vascular pathways with minimal flow resistance could stabilise through inhibition of chemotaxis and therefore mimic the quiescent cellular state found in mature vascular networks [3] with differentiation between capillaries, arterioles and venules. Analysis of vessel thickness will be performed to see if it corresponds with in vivo observations of mature vascular networks.

3.3.1 Parameters

To investigate the role that molecular mechanisms potentially play in stabilisation of the vascular network after the formation of the primitive plexus, we run simulations with variations in parameters that influence the inhibition of chemotaxis by flow. Ten simulations were run under different seeds for each parameter configuration.

Tuning χ is independent of flow sensing, instead it adjusts the strength of the chemotactic response. Values tested for are 1000 and 4000.

The value of ζ is set such that when fluidic velocity, in the unit of lattice sites per MCS, equals ζ the cells become completely insensitive to chemotaxis. Setting ζ to an infinitesimal number implies that throughout the vasculature the ECs would be hypersensitive to flow velocity and fully suppress chemotaxis. An infinite value would imply no suppression of chemotaxis by all cells. Biologically, ζ could be thought of as a mechanosensitive transcription factor. Values tested for are 10 for minimal inhibition, 5 for strong inhibition and infinity for chemotaxis being independent of flow.

The value of 10 m s^{-1} will be tested for to investigate how the vasculature is affected when the maximal inhibition value is not far off (± 5) from maximal velocity values expected to be reached, $\zeta = 5 \text{ m s}^{-1}$ will be tested to investigate strong dependence of chemotaxis inhibition on flow, finally the computational equivalent of infinity is tested for to investigate the default case of flow independent chemotaxis. Altogether, the parameter combinations of the cartesian product of the values of ζ and χ will be analysed

3.3.2 Analysis

Figure 9 shows how flow drives an hierarchy in vessel thickness. It arises from an initially preferable passage of flow between the low and high pressure walls of the tissue engineering environment. The increased flow results in quiescence of the associated cells by means of flow induced chemotactic inhibition, such that ECs start to accumulate. The chemotaxis sensing activity scales inversely linearly with flow velocity which means that cells in high flow segments still show motility with respect to adhesion energies and area and length constraints, yet the chemotaxis component plays a lesser role. As such, any smaller vessel that might be situated between the high VEGF secreting blood islands, as the rate of VEGF secretion scales with EC quantity, might in the flow-independent chemotaxis scenario be broken up through the chemotactic pull from both sides. If these smaller vessel segments act as an important passage of blood flow, higher WSS will be sensed, approximated in our model by flow velocity. This might inhibit the splitting up of the smaller vessel and consecutive migrating towards its neighbouring EC/VEGF islands.

The still motile cells in neighboring capillaries are in addition attracted to the high levels of VEGF (this can be observed in the figure by the bright green contour lines that encapsulate the high flow vessels, where brightness scales with concentration) being exuded from the thickening vessels. From the Hagen-Poiseuille equation we know that volumetric flow rate scales with the vessel thickness to the fourth power. The result is a positive feedback loop between high flow and thickening of vessels through EC accumulation and attraction, which leads to stabilisation of the high flow vessel segments.

Interestingly, research by Iizuka et al. [38] on the retina of mouse models at postnatal day 5-8 has investigated the relationship between theoretical expectations and experimental data. The theoretical postulations were based on Murray’s law, which predicts the thickness of vascular branches in terms of metabolic optimisation ¹. Murray’s law states that the relationship between a parent vessel r and its n child branches, see equation 10.

$$r^3 = r_1^3 + r_2^3 + \dots + r_n^3 \quad (10)$$

Figure 11 shows the power coefficient, whilst plotting the vessel thickness over count, dropping from -3.5 at the immature vascular plexus to -1.6 with a more mature vasculature. A coefficient of -3 is expected under Murray’s law when all vessels have a bifurcation of two, a lower average bifurcation number would decrease the value of this coefficient as it would diminish the numbers of smaller vessel segment. Similar droppings of the coefficient can be observed in Figure 12. The power law relationship becomes less well defined when chemotaxis is dependent on flow, this stands in contrast to the results of Figure 11, where the R^2 factor increases. This suggests that the phenomenon that we observe might not necessarily be metabolic optimisation, specified by the change in radius at vascular bifurcation sections as specified by Murray’s law. To achieve such a result, oxygenation factors would have to be taken into account in the model. In contrast, the model focusses on stabilisation of high flow vessel segments. Observing Figure 10 shows indeed a strong differentiation between small and thick vessel segments due to the increase in thickness of any initially preferable passages of blood. In Figure 13 we can indeed observe, especially for $\zeta = 4000 \text{ m s}^{-1}$, a clustering between small (arteries) and thick vessel segments (arterioles). The plot shows the mean radius over 9 different runs combined, as well as the mean over all segments with radius either below or above that. The difference between these means, the IMR, is distinctly bigger when chemotaxis is inhibited by flow. As such, the plots confirm a significant differentiation into arteries and arterioles as all p-values are significant with $\alpha = 0.5$, using Welch’s t-test (this test is used due to the assumption of differing variance between the compared samples).

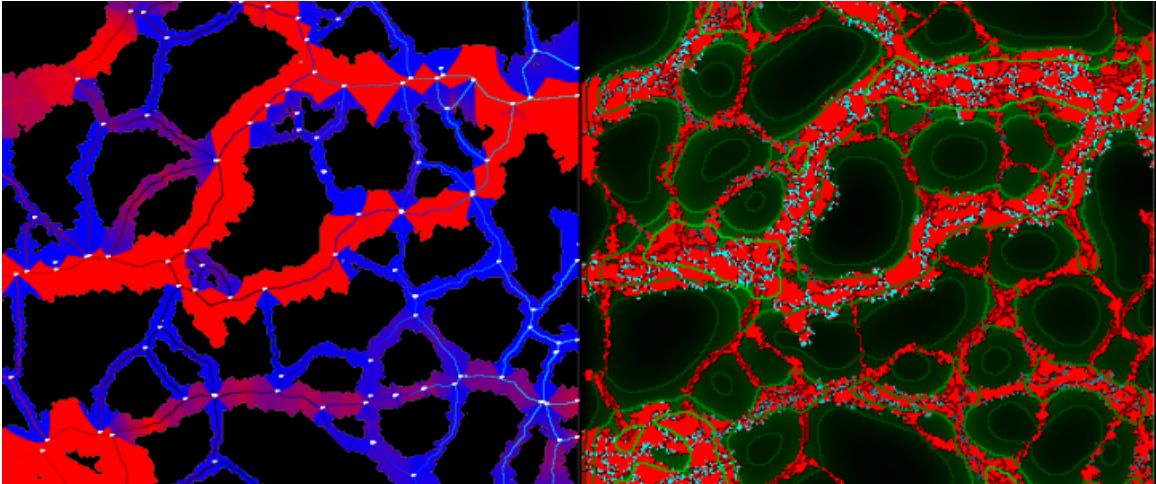


Figure 9. Flow-inhibited chemotaxis creates a positive feedback loop between vessel size and flow. At MCS 200 ($\chi = 1000, \zeta = 4000 \text{ m s}^{-1}$) the stabilisation of high-flow segments through flow-inhibited chemotaxis is already observable. High flow velocities maps onto high amount of chemotaxis repression, shown through the blue coloured membrane loci, where the brightness scales linearly with inhibition strength. The thickest segments show maximal repression.

¹Like the Hagen-Poiseuille equation, Murray’s law was formulated in a biological context with respect to the vascular system, but proved to be basic physical principles; Murray’s law can be generalized according to the minimisation of transport and maintenance costs in the context of transport networks.

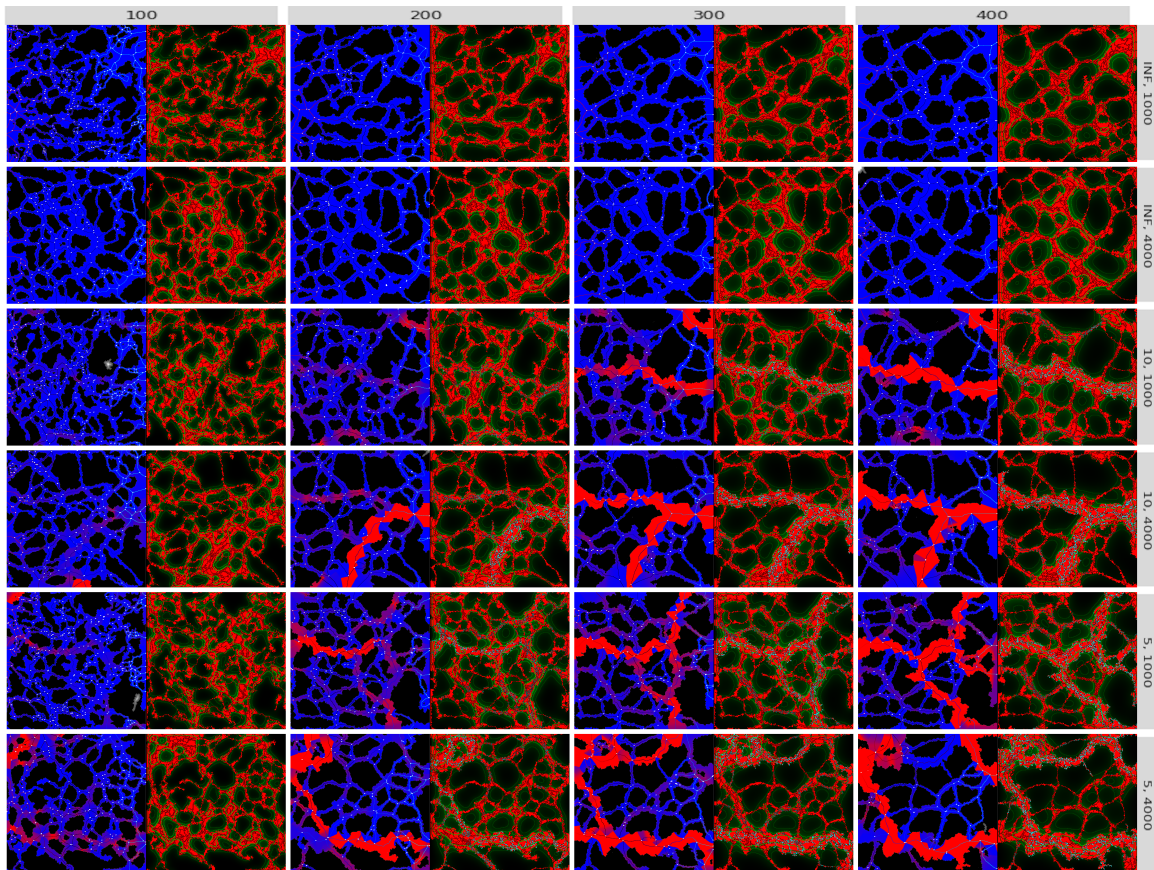


Figure 10. Clear differentiation arises between flow independent and dependent vascular remodelling. The development of the simulated vasculature over MCS 100 to 400, in intervals of 100, is shown over the columns. Parameters over the rows are (χ, ζ) . Increasing the maximal inhibition velocity and chemotaxis strength results in faster remodelling, as can be seen by comparing row 3 with 6. Independence on flow (row 1, 2) does not cluster the vasculature, in contrast to dependent chemotactic sensing, in small and thick vessels.

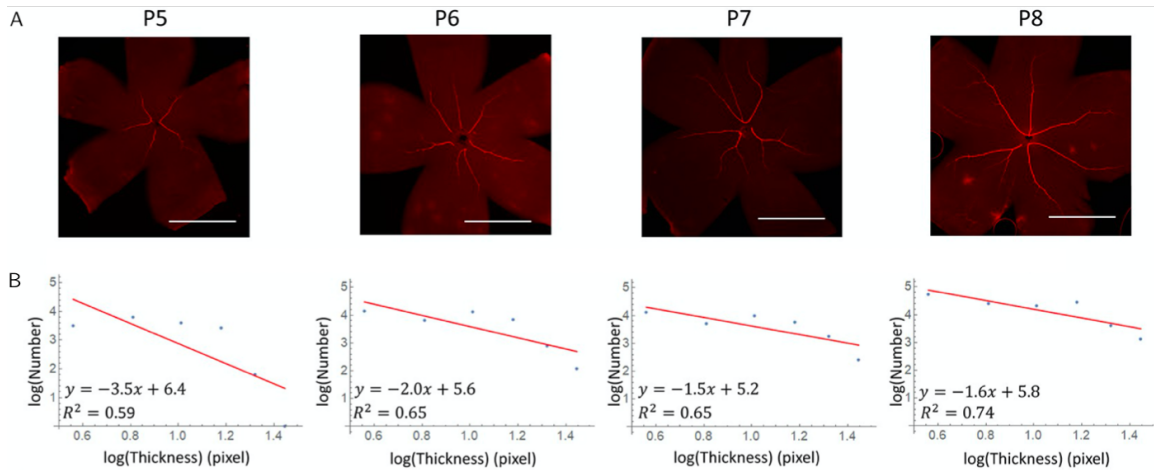


Figure 11. As the vasculature matures the accumulation of thicker vessels leads to a decreasing coefficient in the log-log plot relating vessel thickness to count. The expected relationship between the logarithm of both vessel thickness and count should be the power law of 2^{-3} according to Murray's law, where the value of 2 assumes that each branching event can be classified as a bifurcation. If a hierarchy of decreasing vessel thickness is envisioned that adheres to this law we should see 2^{n+1} vessels with radius $2^{-1/3}r_n$ originating from the bifurcation of the 2^n preceding vessels of radius r_n . The coefficient becomes 3 when plotting with the radius as independent value. **(A)** Plotted are observations from mice retina, over postnatal day 5, 6, 7 and 8 [38]. **(B)** The decreasing coefficient, found after segmenting and analysing the experimental data [38] from the postnatal day associated to the column, might be explained if thick vessels do not always branch into two smaller vessels but at times branch into one smaller vessel and continue with equal radius on the 2nd branch, which is what occurs with primary vessels that show many side branches.

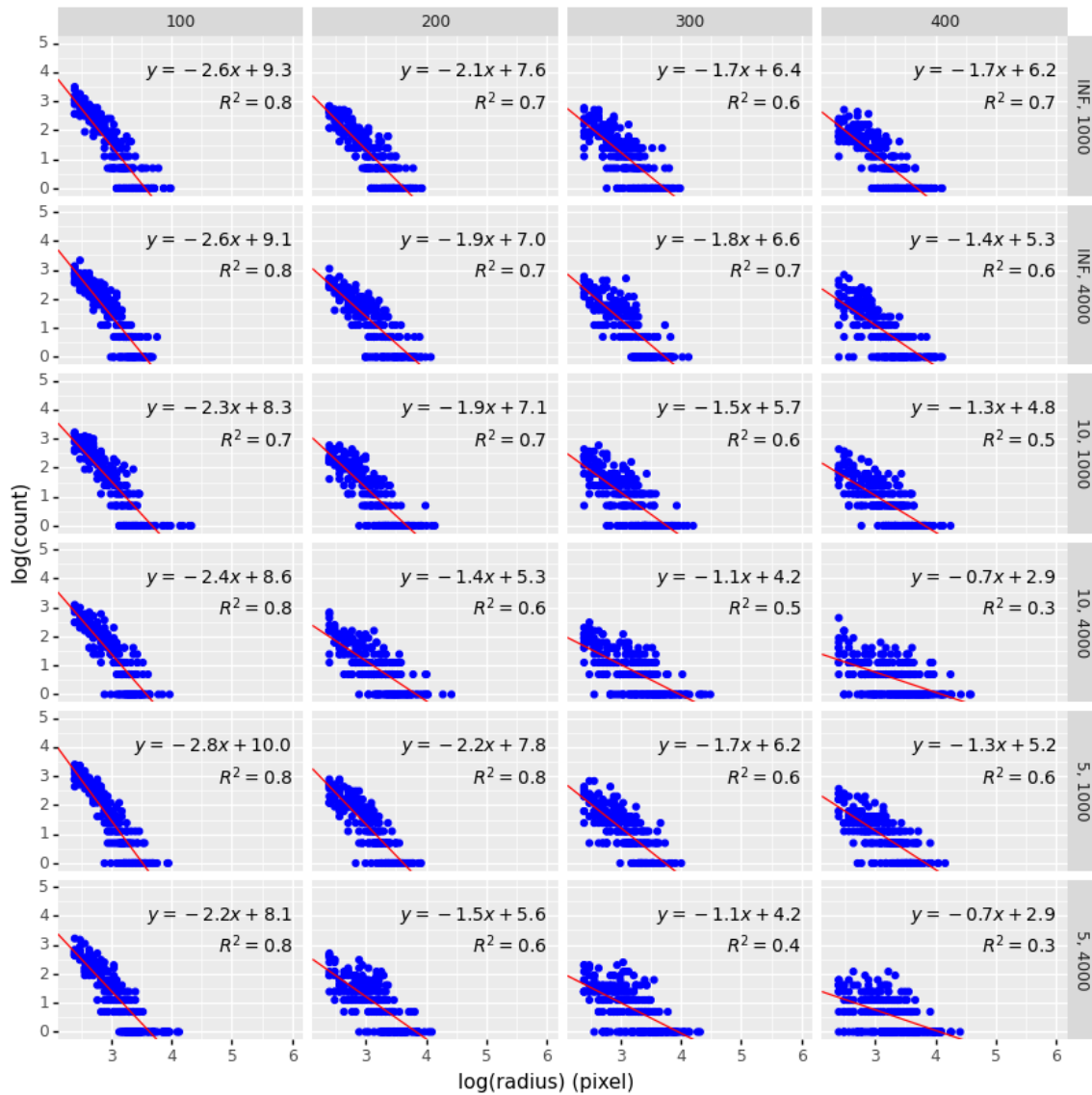


Figure 12. Flow-inhibited chemotaxis leads to deviations from Murray's law. The counts of the mean vessel segments radius are plotted, where we define a vessel segment as the vascular segments associated to an edge situated between two nodes, as such the thicker continuous vessels that span over the lattice consist of multiple vessels segments. Results are aggregated from 9 simulation runs, where for each run and radius we plot the observed count as a point, under different seeds. Results with dependence of chemotaxis on flow are compared against results with equal MCS and χ , yet with independence on flow as indicated by values of infinity for ζ . For example the p value of row 5 column 3 is compared against row 1 column 3. Row 6 column 4 against row 2 column 4. The slope decreases for all simulations as the simulation progresses. With a more aggressive slope and loss of the power law relationship when ζ equals 4000. The declining slope can be explained by the increase in count of thicker vessel segments and the observation from Figure 10 that thicker vessels show many side branches, whereas the non-remodelled segments show more bifurcations in smaller sections adhering to Murray's law.

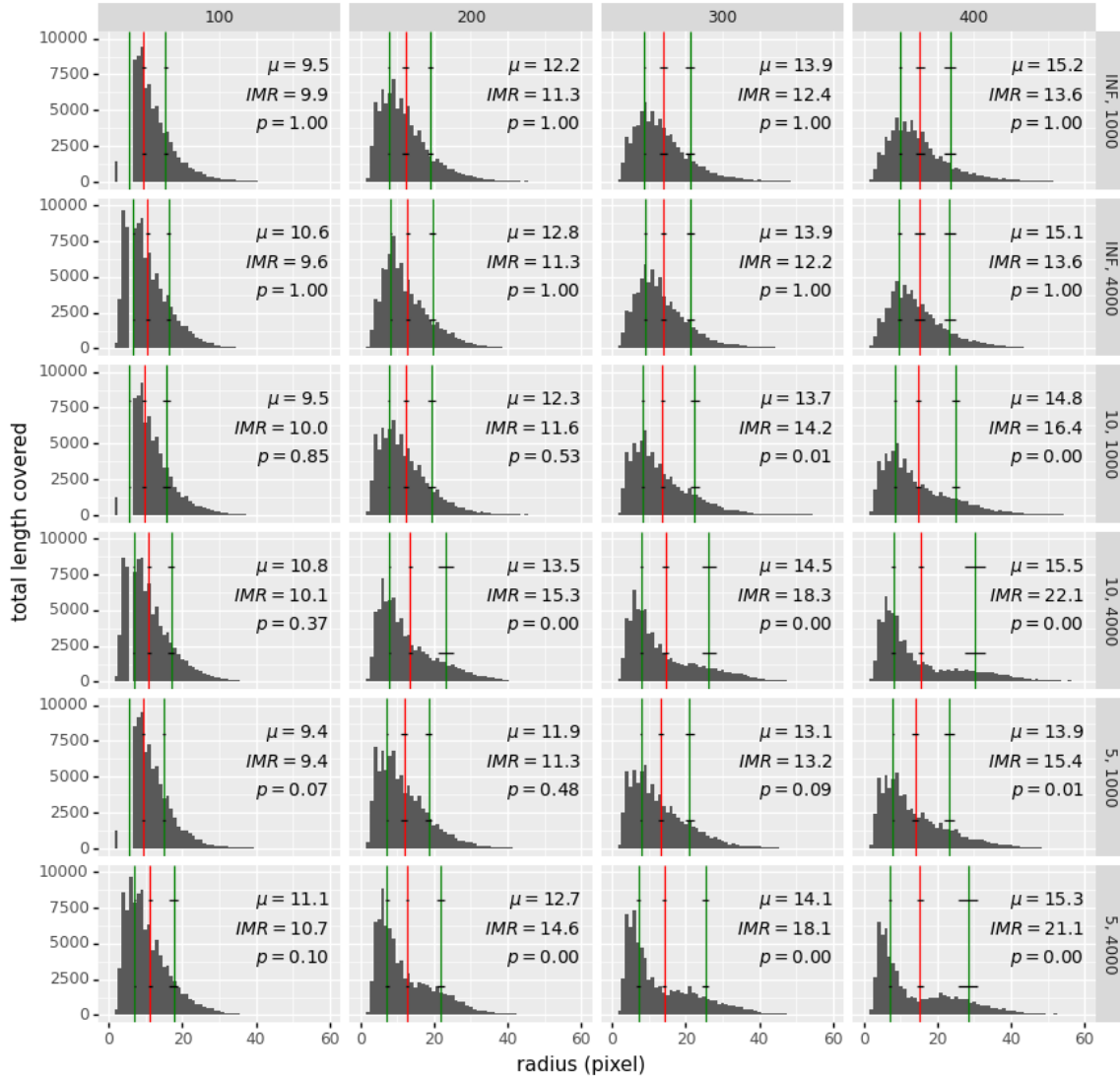


Figure 13. Clustering occurs between capillaries and equivalents of arterioles. The total length covered by different radii are plotted, where the results are aggregated from 9 simulation runs under different seeds. Mean values of the vessel radius (red), with radius calculated at each lattice site along the midline of the vessel, do not show significant difference between flow dependent and independent chemotaxis. Yet, the difference between the mean value (green) of the upper half of the total mean and the mean value of the lower half of the lower mean (which we abbreviate to IMR) seems to indicate that the vessels tend to differentiate themselves more into either thin or thick vessels. The p-value confirms that this behaviour is significantly different between the dependent and independent mode.

4 Discussion

The results show that the skeleton which is needed for graph extraction and haemodynamic calculation can be efficiently and dynamically updated. In addition, although the power law relationship did not hold for flow inhibited chemotaxis there was a clear differentiation established between smaller and larger vessels, which was not present in the flow-independent condition. ECs take on a quiescent condition in the high flow segments. Thus, our research suggests that flow-based inhibition of chemotaxis can result in functional vascular stabilisation through high flow vessel segments showing low EC motility and smaller vessels having high motility. Migration is not directional, but there remains an inflow of ECs from the small high motility vessels into the high flow and larger vessels. The larger vessels, possibly functioning as arterioles, act as stable vessels that span over the CPM lattice and show a high volume flow rate. Thereby they can fulfill important roles in metabolically supplying the vasculature.

We suggest possible biological mechanisms that might induce the flow-based inhibition of chemotaxis. Coupling of a WSS sensing complex with a modulator of chemotaxis sensitivity might make cells, under the influence of WSS, less sensitive towards chemical signalling molecules. Glycocalyx and embedded glycoproteins on the luminal membrane [19] and VE-cadherin, VEGFR2 and PECAM1 [16] sense and relay forces. The relayed forces are then potentially coupled to the chemotaxis modulators NO, influencing vasodilation, and/or ROS, which affects VEGF-induced autophosphorylation of VEGFR-2 [19]. Decreasing VEGF receptor sensitivity is another potential mechanism. Additionally, VE-cadherin is a potential candidate that might mediate the flow-repressed chemotaxis, as the protein is both involved in chemotaxis, where it dissociates from β -catenin in response to VEGF, as well as transmission of shear stress signals. It can be postulated that biological mechanisms have build in protective measurements to prevent VE-cadherin dissolution at moments when other components are dependent on its proper functioning, such as during shear stress modulation. If it fails to dissociate during high WSS it will not be susceptible to VEGF influences [19].

Results differ from stabilisation of the inner positioned ECs through contact-inhibition, which stabilises the inner ECs and potentially leads to blood island formation [27]. Due to the locality of contact inhibition, it stands in contrast to the global effects of flow-dependent inhibition, where stabilisation occurs collectively in the vessels which promote blood flow throughout the vasculature. In contact-inhibition the invading chemotaxis sensing cell at the periphery displace the interior cells, whereas with flow-inhibited chemotaxis no distinction is made between central and peripheral cells. Runs with flow-independence did also not show blood island formation, possibly this would have occurred when the simulation was run for more MCSs. Halting the algorithm until stabilisation is suggested for a future work. The conceptual CPM model of vasculogenesis by Merks et al. [21] and Daub and Merks [39] has been expanded upon with the implementation of flow dynamics in the CPM model.

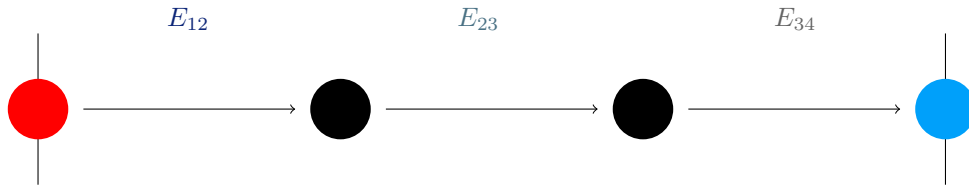
Future work could, in addition, implement dynamic viscosity for a more realistic simulation. Currently, this value is set to a constant, but it ought to vary over vessel radius. Decreasing inversely with the radius until it reaches a small enough radius that it start to rise again. No slip conditions at the vessel lining and plasma skimming would be other, more advanced, facets adding to the realism. In addition, computationally gains can be made through applying methods as Successive Over Relaxation for solving the inverse of the matrices. The simulations would also benefit from being halted when they stabilise instead of a predefined number. Finally, metabolism is not modelled, doing so could lead to investigations on the influence of oxygenation, such as fewer vessels branching points closer to oxygen rich areas. Thereby creating larger lacuna in the proximity of the arterioles [38]. Shear stress could also be used as a more biologically accurate sensing of flow as opposed to flow velocity. Graph theory could be applied on the vascular network to uncover for example hidden abstractions of the graph such as the small-world phenomenon in which any tissue cell can be metabolically affected by every other tissue cell by a small number of steps, which might be of importance within the concept of tumour metastasis. In addition, differences in vascular structure, for example the density of nodes, is expected to differ dependent on the distance from the arterioles as tissues distal from high flow segment are expected to be more hypoxic and thus induce more explorative sprouting behaviour. Future work should clarify differences between WSS mediated inhibition of chemotaxis and WSS driven changes in cellular junctions [25], where both are flow-based approaches that influence cellular motility. Other hypotheses to be explored are whether the influence of shear stress on the stress fibers might induce favourable or unfavourable changes in cell shape with respect to motility and thereby influence vascular stabilisation. Or, the influence of shear stress on cell polarisation, which could influence cells to migrate with directional persistence up the flow gradient.

References

- [1] Sybill Patan. “Vasculogenesis and angiogenesis as mechanisms of vascular network formation, growth and remodeling”. In: *Journal of neuro-oncology* 50.1 (2000), pp. 1–15.
- [2] Nuria Martinez-Martin et al. “Metabolomics of the effect of AMPK activation by AICAR on human umbilical vein endothelial cells”. In: *International journal of molecular medicine* 29.1 (2012), pp. 88–94.
- [3] Frederik De Smet et al. “Mechanisms of vessel branching: filopodia on endothelial tip cells lead the way”. In: *Arteriosclerosis, thrombosis, and vascular biology* 29.5 (2009), pp. 639–649.
- [4] Catarina G Fonseca, Pedro Barbacena, and Claudio A Franco. “Endothelial cells on the move: dynamics in vascular morphogenesis and disease”. In: *Vascular Biology* 2.1 (2020), H29–H43.
- [5] Claudio A Franco et al. “Dynamic endothelial cell rearrangements drive developmental vessel regression”. In: *PLoS biology* 13.4 (2015), e1002125.
- [6] Barbara Muz et al. “The role of hypoxia in cancer progression, angiogenesis, metastasis, and resistance to therapy”. In: *Hypoxia* 3 (2015), p. 83.
- [7] Martin A Schwartz, Dietmar Vestweber, and Michael Simons. “A unifying concept in vascular health and disease”. In: *Science* 360.6386 (2018), pp. 270–271.
- [8] Claudio A Franco et al. “Non-canonical Wnt signalling modulates the endothelial shear stress flow sensor in vascular remodelling”. In: *Elife* 5 (2016), e07727.
- [9] Ralf Gödde and Haymo Kurz. “Structural and biophysical simulation of angiogenesis and vascular remodeling”. In: *Developmental dynamics: an official publication of the American Association of Anatomists* 220.4 (2001), pp. 387–401.
- [10] M Welter and H Rieger. “Physical determinants of vascular network remodeling during tumor growth”. In: *The European Physical Journal E* 33.2 (2010), pp. 149–163.
- [11] Michael Simons and Anne Eichmann. “Molecular controls of arterial morphogenesis”. In: *Circulation research* 116.10 (2015), pp. 1712–1724.
- [12] Miguel O Bernabeu et al. “Computer simulations reveal complex distribution of haemodynamic forces in a mouse retina model of angiogenesis”. In: *Journal of The Royal Society Interface* 11.99 (2014), p. 20140543.
- [13] Yuki Wakayama et al. “Cdc42 mediates Bmp-induced sprouting angiogenesis through Fmnl3-driven assembly of endothelial filopodia in zebrafish”. In: *Developmental cell* 32.1 (2015), pp. 109–122.
- [14] Peter Carmeliet. “Angiogenesis in life, disease and medicine”. In: *Nature* 438.7070 (2005), pp. 932–936.
- [15] Cornelia Hahn and Martin A Schwartz. “Mechanotransduction in vascular physiology and atherogenesis”. In: *Nature reviews Molecular cell biology* 10.1 (2009), pp. 53–62.
- [16] Eleni Tzima et al. “A mechanosensory complex that mediates the endothelial cell response to fluid shear stress”. In: *Nature* 437.7057 (2005), pp. 426–431.
- [17] Hiroyuki Nakajima et al. “Flow-dependent endothelial YAP regulation contributes to vessel maintenance”. In: *Developmental cell* 40.6 (2017), pp. 523–536.
- [18] Mariona Graupera et al. “Angiogenesis selectively requires the p110 α isoform of PI3K to control endothelial cell migration”. In: *Nature* 453.7195 (2008), pp. 662–666.
- [19] Laurent Lamallice, Fabrice Le Boeuf, and Jacques Huot. “Endothelial cell migration during angiogenesis”. In: *Circulation research* 100.6 (2007), pp. 782–794.
- [20] Dimitrios Palachanis, András Szabó, and Roeland MH Merks. “Particle-based simulation of ellipse-shaped particle aggregation as a model for vascular network formation”. In: *Computational Particle Mechanics* 2.4 (2015), pp. 371–379.
- [21] Roeland MH Merks et al. “Cell elongation is key to in silico replication of in vitro vasculogenesis and subsequent remodeling”. In: *Developmental biology* 289.1 (2006), pp. 44–54.
- [22] François Pouthas et al. “In migrating cells, the Golgi complex and the position of the centrosome depend on geometrical constraints of the substratum”. In: *Journal of cell science* 121.14 (2008), pp. 2406–2414.

- [23] Miguel O Bernabeu et al. “PolNet: A tool to quantify network-level cell polarity and blood flow in vascular remodeling”. In: *Biophysical journal* 114.9 (2018), pp. 2052–2058.
- [24] Akira Katsumi et al. “Integrins in mechanotransduction”. In: *Journal of Biological Chemistry* 279.13 (2004), pp. 12001–12004.
- [25] Daniel E Conway et al. “Fluid shear stress on endothelial cells modulates mechanical tension across VE-cadherin and PECAM-1”. In: *Current Biology* 23.11 (2013), pp. 1024–1030.
- [26] Sylvie Gory-Fauré et al. “Role of vascular endothelial-cadherin in vascular morphogenesis”. In: *Development* 126.10 (1999), pp. 2093–2102.
- [27] Roeland MH Merks et al. “Contact-inhibited chemotaxis in de novo and sprouting blood-vessel growth”. In: *PLoS computational biology* 4.9 (2008), e1000163.
- [28] Stanley E Charm and George S Kurland. *Blood flow and microcirculation*. Wiley, 1974.
- [29] Alexander RA Anderson and Mark A J Chaplain. “Continuous and discrete mathematical models of tumor-induced angiogenesis”. In: *Bulletin of mathematical biology* 60.5 (1998), pp. 857–899.
- [30] Roeland MH Merks and James A Glazier. “A cell-centered approach to developmental biology”. In: *Physica A: Statistical Mechanics and its Applications* 352.1 (2005), pp. 113–130.
- [31] François Graner and James A Glazier. “Simulation of biological cell sorting using a two-dimensional extended Potts model”. In: *Physical review letters* 69.13 (1992), p. 2013.
- [32] Katherine Holmes et al. “Vascular endothelial growth factor receptor-2: structure, function, intracellular signalling and therapeutic inhibition”. In: *Cellular signalling* 19.10 (2007), pp. 2003–2012.
- [33] D Ambrosi, A Gamba, and G Serini. “Cell directional persistence and chemotaxis in vascular morphogenesis”. In: *Bulletin of Mathematical Biology* 67.1 (2005), pp. 195–195.
- [34] Josephine T Daub and Roeland MH Merks. “Cell-based computational modeling of vascular morphogenesis using Tissue Simulation Toolkit”. In: *Vascular morphogenesis*. Springer, 2015, pp. 67–127.
- [35] Holger Gerhardt et al. “VEGF guides angiogenic sprouting utilizing endothelial tip cell filopodia”. In: *The Journal of cell biology* 161.6 (2003), pp. 1163–1177.
- [36] Nicholas J Savill and Paulien Hogeweg. “Modelling morphogenesis: from single cells to crawling slugs”. In: *Journal of theoretical biology* 184.3 (1997), pp. 229–235.
- [37] Boris Lau, Christoph Sprunk, and Wolfram Burgard. “Improved updating of Euclidean distance maps and Voronoi diagrams”. In: *2010 IEEE/RSJ International Conference on Intelligent Robots and Systems*. IEEE. 2010, pp. 281–286.
- [38] Osamu Iizuka et al. “Remodeling mechanisms determine size distributions in developing retinal vasculature”. In: *PloS one* 15.10 (2020), e0235373.
- [39] Josephine T Daub and Roeland MH Merks. “A cell-based model of extracellular-matrix-guided endothelial cell migration during angiogenesis”. In: *Bulletin of mathematical biology* 75.8 (2013), pp. 1377–1399.

Appendix A: Nodal Admittance Matrix Example



1. Apply nodal flow conditions:

$$\begin{cases} Q_{21} + Q_{23} & = 0 \\ Q_{32} + Q_{34} & = 0 \\ G_{12}\Delta p_{21} + G_{23}\Delta p_{23} & = 0 \\ G_{23}\Delta p_{32} + G_{34}\Delta p_{34} & = 0 \end{cases}$$

2. Transfer vessel conductivity and nodal pressure values to matrix:

$$\begin{bmatrix} n_1 & n_2 & n_3 & n_4 \\ n_2 & -G_{12} & G_{12} + G_{23} & -G_{23} \\ n_3 & & -G_{23} & G_{23} + G_{34} \\ & & & -G_{34} \end{bmatrix} \cdot \begin{bmatrix} p \\ 1 \\ p_2 \\ p_3 \\ 0 \end{bmatrix} = \vec{0}$$

3. Rearrange:

$$\begin{bmatrix} n_2 & n_3 \\ n_2 & G_{12} + G_{23} & -G_{23} \\ n_3 & -G_{23} & G_{23} + G_{34} \end{bmatrix} \cdot \begin{bmatrix} p \\ p_2 \\ p_3 \end{bmatrix} = \begin{bmatrix} rhs \\ G_{12} * 1 \\ G_{34} * 0 \end{bmatrix}$$

4. Solve for nodal pressure values.

Supplements

Code can be accessed from:

https://github.com/richardkok14/CPM_haemodynamics